THE JOURNAL OF PHYSICAL CHEMISTRY A

Article

Cite This: J. Phys. Chem. A 2019, 123, 7881−7891

pubs.acs.org/JPCA

Symmetry-Adapted Perturbation Theory Decomposition of the Reaction Force: Insights into Substituent Effects Involved in Hemiacetal Formation Mechanisms

Wallace D. Derricotte*

Department of Chemistry, Morehouse College, Atlanta, Georgia 30314, United States

Supporting Information

ABSTRACT: The decomposition of the reaction force based on symmetry-adapted perturbation theory (SAPT) has been proposed. This approach was used to investigate the substituent effects along the reaction coordinate pathway for the hemiacetal formation mechanism between methanol and substituted aldehydes of the form CX_3CHO (X = H, F, Cl, and Br), providing a quantitative evaluation of the reaction-driving and reaction-retarding force components. Our results highlight the importance of more favorable electrostatic and induction effects in the reactions involving halogenated aldehydes that leads to lower activation energy barriers. These substituent effects are further elucidated by applying the functional-group partition of symmetry-adapted perturbation theory (F-SAPT). The results show that the reaction is largely driven by favorable direct noncovalent interactions between the CX_3 group on the aldehyde and the OH group on methanol.

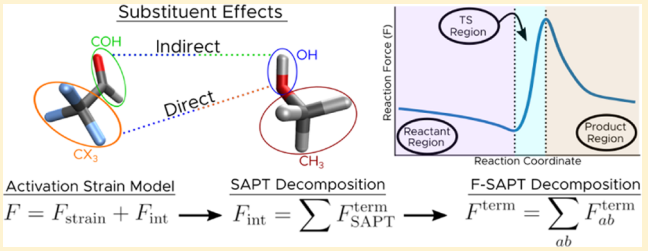

1. INTRODUCTION

Having an in-depth understanding of the reaction mechanisms that drive chemical and physical transformations can aid in manipulation of these processes toward the design of new, more efficient reactions. These processes are often governed by the propensity of molecules to react and form new species. Many significant scientific challenges and new technological advancements depend on an elementary understanding of fundamental chemical processes, for example, the design of efficient catalytic reactors that depends on a fundamental understanding of catalysis,[1,2] genetic engineering that depends on the understanding of biosynthetic pathways,[3] and numerous technological advances that hinge on the design and production of new materials.[4−7] Computational quantum chemistry can be particularly helpful in obtaining key insight into chemical reactions. Many theories arising from this field, such as Marcus theory,[8] valence-bond theory,[9] and frontier molecular orbital theory,[10] have transformed our understanding of chemical reactions and are even routinely applied by experimentalists.

Although general trends in chemical reactivity may be explained with simple chemical intuition, when this intuition is combined with modern quantum chemistry calculations, it is possible to provide fundamental explanations based on a detailed understanding of the changes in electronic structure.[11−13] The progress of a chemical reaction can be modeled computationally by considering the variation of the potential energy of the system with respect to nuclear motion along a well-defined pathway from reactants to products. One such path can be obtained from the intrinsic reaction coordinate (IRC) pioneered by Fukui et al., which provides an explicit one-dimensional coordinate that summarizes the minimum energy path for a chemical reaction.[14] Efforts by the research group of Alejandro Toro-Labbé have shown that additional information can be gleaned from examining the derivative of the energy along the IRC, introducing a concept known as the reaction force.[15−18] Analogous to the classical force, the reaction force is defined as the negative energy gradient with respect to the reaction coordinate. Fundamentally, the reaction force allows for a practical partitioning of the reaction coordinate into three regions (shown visually in Figure 1): (1) a reactant region associated with geometrical changes necessary to form the transition state (TS) structure, (2) the TS region associated with the reorganization of the electron density, and (3) the product region associated with the geometrical relaxation of the TS to form the final product. This general framework for partitioning the reaction inspired further developments, leading to investigation of the second energy derivative along the IRC known as the reaction force constant[19,20] as well as the derivative of the electronic chemical potential known as the reaction electronic flux.[21−24] Together, these properties have been proven useful in providing new chemical insight in a wide variety of reaction mechanisms.[25−44]

In addition to properties based on the total energy, fragment-based approaches strive to provide additional insight by partitioning the chemical system into interacting monomers and describing the height of the activation energy barrier in terms of modulations of the original reactants. This idea was

Received: July 18, 2019
Revised: August 19, 2019
Published: August 20, 2019

DOI: 10.1021/acs.jpca.9b06865
J. Phys. Chem. A 2019, 123, 7881−7891

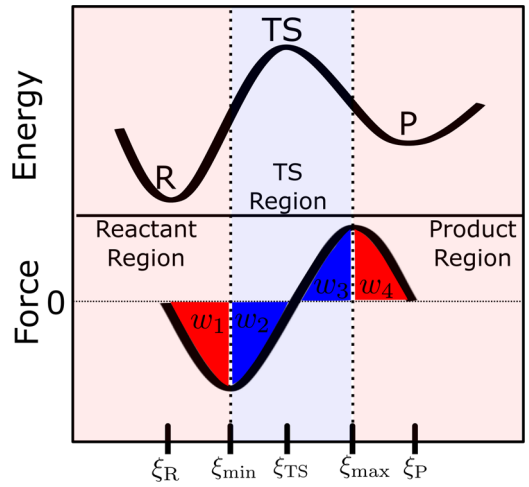

Figure 1. Schematic showing the relationship between reaction energy, reaction force, and reaction work. (See text for more detail.)

spearheaded by Morokuma in the early 1970s where he utilized energy decomposition schemes to analyze energy and force components for stable molecules.[45,46] More recently, the activation strain model (ASM),[47,48] also known as the distortion/interaction model,[49] has established a unique approach to understanding chemical reactivity by establishing a causal relationship between the reaction energy barriers and the properties/characteristics of reactants involved in reaction mechanisms.[50] This model employs a simple partitioning scheme in which the potential energy is decomposed into two contributions along the reaction coordinate: (1) the strain energy that is associated with the structural deformation of the reactant geometries and (2) the electronic interaction between the reactants. The electronic interaction component is further decomposed using the Kohn−Sham molecular orbital theory into components from electrostatics, Pauli repulsion, and orbital interactions.[51] This ASM approach has been successful in uncovering the physical factors controlling activation barriers in numerous fundamental chemical processes, including nucleophilic substitution,[50,52−54] oxidative addition,[55,56] perycyclic reactions,[57−59] and unimolecular rearrangements.[60,61]

Recently, energy decomposition analysis (EDA) techniques have been applied within the context of the ASM and reaction force analysis. EDA techniques can be classified based on the underlying theory that produces the decomposition. One class of EDA techniques is known as variational EDA in which the energy is decomposed by variational treatment of the intermediate wavefunctions. The other class is perturbation-based EDA in which the interaction between two monomers is calculated as a perturbation to the noninteracting Hamiltonian; within this context the different terms of the perturbation series correspond to physically relevant decomposition of the interaction energy. Efforts from the groups of Alejandro Toro-Labbé and Artur Michalak have focused on decomposition of the reaction force using the extended transition state (ETS) variational EDA technique[62−64] combined with analysis of the electron density changes based on natural orbitals for chemical valence (NOCV),[65,66] in the ETS-NOCV approach.[40,67−69] Their work highlights the utility of characterizing the driving and retarding intermolecular forces throughout a chemical reaction in the cases of the water-assisted HCN/CNH isomerization,[70] metal-assisted intramolecular proton transfer in thymine,[71] and double proton transfer in formamide-derived complexes.[72] To our knowledge, there have been no studies exploring the use of a perturbative approach for the decomposition of the reaction force.

The most pervasive perturbative EDA approach is symmetry-adapted perturbation theory (SAPT).[73] Within SAPT, the interaction energy is treated as a perturbative expansion where the first few terms correspond to a physically relevant decomposition of the interaction energy into contributions from electrostatics, exchange-repulsion, induction, and dispersion. The electrostatic term can be understood as a simple classical interaction involving the static charge distributions of two interacting monomers. Induction effects emerge from the response of one monomer due to the electric field of the other. Contributions from dispersion arise due to fluctuations in the charge distributions of the two monomers resulting from the correlation of their electrons. Exchange repulsion occurs because of the overlap of molecular wavefunctions; as electrons are free to move across both monomers there is an energy penalty associated with maintaining the antisymmetry condition of the total wavefunction. Recent efforts by Sherrill et al. have focused on the chemically motivated assignment of the SAPT energy terms to interactions between atoms or functional groups resulting in the atomic[74] and functional-group[75] SAPT partitions (A-SAPT and F-SAPT, respectively). These robust partitions of SAPT provide explicit quantification of the intermolecular forces between specific consituents of each monomer.

The applicability of SAPT has grown significantly over the last decade due to algorithmic advances, including density-fitting and Cholesky decomposition of the two-electron integrals,[76−78] natural orbital truncations of the virtual orbital space,[79,80] and efficient implementations on graphical processing units.[81] The applications of SAPT and its atomic- and functional-group variants have been utilized in a diverse span of applications, including π interactions in conjugated systems,[82] ligand−protein interactions,[81,83] analysis of transition-state stabilization,[84,85] the development of so-called "next-generation" ab initio force fields for molecular dynamics,[86−90] and many others[91−99]

The primary goal of this work is to extend the activation strain energy partitioning of the reaction force analysis by further decomposition of the interacting force using SAPT and F-SAPT. This approach is utilized to study the substituent effects on the reaction mechanism of hemiacetal formation between methanol (CH_3OH) and aldehydes of the form CX_3CHO (X = H, F, Cl, Br). This reaction is characterized by two chemical events that occur simultaneously: (1) the oxygen atom of the hydroxyl group of methanol attacks the carbonyl carbon of the aldehyde and (2) the hydrogen atom of the hydroxyl group is donated to the carbonyl oxygen forming the final hemiacetal structure. This class of reactions has been studied extensively in the literature;[100−104] a computational study specifically investigating the substituent effects comparing acetaldehyde (X = H) with fluoral (X = F), chloral (X = Cl), and bromal (X = Br) group was carried out by Azofra et al.[105] Their results showed the smallest energy barrier for fluoral, followed by chloral, bromal, and then acetaldehyde group. They rationalize this by establishing a linear correlation between the relative nucleophilicity of the carbonyl carbon atom and the activation energy barrier. This rationalization implies that the primary substituent effect is an indirect effect; i.e., the electron-withdrawing substituents pull electron density

DOI: 10.1021/acs.jpca.9b06865
J. Phys. Chem. A 2019, 123, 7881−7891

from the carbonyl facilitating a more favorable interaction between the carbonyl and the hydroxyl group. Making use of the F-SAPT partition, we will explicitly investigate the substituent effect of the CX_3 group and quantify its effect on the activation energy barrier.

2. THEORETICAL BACKGROUND

2.1. Energy and Reaction Force. The reaction force is defined as the negative gradient of the energy (E) with respect to the reaction coordinate ξ

$$F(\xi) = -\frac{\partial E(\xi)}{\partial \xi} \tag{1}$$

Figure 1 displays a schematic representation of the reaction force along the reaction coordinate ξ and how it corresponds to the energy along the reaction coordinate. For any elementary reaction step, the energy profile establishes three well-defined critical points: two minima that correspond to the reactant (ξ_R) and product (ξ_P) structure and a first-order saddle point that corresponds to the transition-state structure. The reaction force profile $F(\xi)$ establishes two additional critical points along the reaction coordinate, corresponding to the force minimum (ξ_{min}) and force maximum (ξ_{max}). This allows for a rigorous definition of three distinct regions based on this set of critical points: (1) the reactant region ($\xi_R \le \xi \le \xi_{min}$), (2) the transition state region ($\xi_{min} \le \xi \le \xi_{max}$), and (3) the product region ($\xi_{max} \le \xi \le \xi_P$). This partitioning is useful for characterizing which regions along the IRC pathway contribute to key chemical events. Additionally, the activation energy barrier ($\Delta E^{\ddagger}$) can be decomposed into separate contributions from the first two regions[18,106,107]

$$\Delta E^{\ddagger} = [E(\xi_{TS}) - E(\xi_R)] = w_1 + w_2 \tag{2}$$

where w_n is the amount of work done on the system in the n^{th} region of the IRC pathway. These quantities are simply the integral of the force $F(\xi)$ over a given region

$$w_1 = -\int_{\xi_R}^{\xi_{min}} F(\xi)d\xi \; w_2 = -\int_{\xi_{min}}^{\xi_{TS}} F(\xi)d\xi$$
$$w_3 = -\int_{\xi_{TS}}^{\xi_{max}} F(\xi)d\xi \; w_4 = -\int_{\xi_{max}}^{\xi_P} F(\xi)d\xi \tag{3}$$

essentially, this is just the area under the curve of the force (see shaded regions in Figure 1).

2.2. Activation Strain Model. In the activation strain model, reasonable fragments are first chosen as a reference; in typical bimolecular reactions, the choice of fragmentation is the two reactant molecules. The relative energy (ΔE) at any point along the reaction coordinate (ξ) is then split into contributions from a strain energy term (ΔE_{strain}) and an interaction energy term (ΔE_{int})

$$\Delta E(\xi) = \Delta E_{strain}(\xi) + \Delta E_{int}(\xi) \tag{4}$$

The strain energy ΔE_{strain} accounts for the geometrical distortions of the current geometry with respect to the equilibrium geometries of the isolated fragments. Since the geometries have to deform/distort significantly to form the transition-state geometry, this term is generally repulsive. The interaction energy ΔE_{int} takes into account the electronic structure interactions between the fragments and is usually attractive. Early in the reaction coordinate, both of these terms are close to zero since the reactants are minimally distorted and only mildly interacting. As the reaction proceeds, the attractive interaction energy increases in magnitude at a similar rate as the repulsive strain energy.

Recent efforts have focused on the applications of the ASM to reaction force analysis. Given the expression in eq 4, it is possible to define the strain and interaction components of the force

$$F(\xi) = -\frac{\partial \Delta E_{strain}(\xi)}{\partial \xi} - \frac{\partial \Delta E_{int}(\xi)}{\partial \xi}$$
$$= F_{strain}(\xi) + F_{int}(\xi) \tag{5}$$

For interpretation, positive forces are seen as reaction driving whereas negative forces are reaction retarding. Figure 2 shows

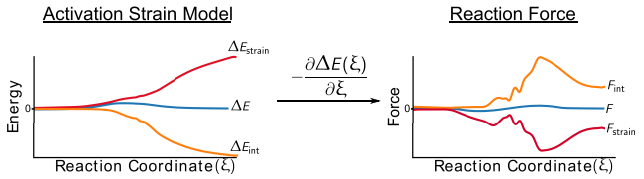

Figure 2. Schematic detailing the idea of combining the reaction force and the activation strain model.

an example of this dynamic. The repulsive strain energy gives rise to a negative/retarding strain force, whereas the attractive interaction energy yields a positive/driving interaction force. Further decomposition of the interaction force (F_{int}) using conventional variational EDA approaches, most notably the ETS-NOCV method, have been explored.[70,72,108]

2.3. SAPT Decomposition of the Reaction Force. Symmetry-adapted perturbation theory (SAPT) allows for the decomposition of the interaction energy into electrostatics (E_{elst}), exchange-repulsion (E_{exch}), induction/polarization (E_{ind}), and dispersion (E_{disp}) components. In this work, it is proposed to incorporate SAPT energy decomposition into the activation strain model

$$\Delta E(\xi) = \Delta E_{strain}(\xi) + \Delta E_{int}^{SAPT}(\xi)$$
$$= \Delta E_{strain}(\xi) + \Delta E_{elst}(\xi) + \Delta E_{exch}(\xi) + \Delta E_{ind}(\xi) + \Delta E_{disp}(\xi)$$

Taking the first derivative of the energy decomposed in this way yields the following decomposition for the reaction force

$$F(\xi) = -\frac{\partial \Delta E_{strain}(\xi)}{\partial \xi} - \frac{\partial \Delta E_{elst}(\xi)}{\partial \xi} - \frac{\partial \Delta E_{exch}(\xi)}{\partial \xi} - \frac{\partial \Delta E_{ind}(\xi)}{\partial \xi} - \frac{\partial \Delta E_{disp}(\xi)}{\partial \xi}$$
$$= F_{strain}(\xi) + F_{elst}(\xi) + F_{exch}(\xi) + F_{ind}(\xi) + F_{disp}(\xi) \tag{6}$$

Integrating over the force components for any region defined between points ξ_1 and ξ_2 can also yield decomposition of the work as well

$$w = -\int_{\xi_1}^{\xi_2} F_{strain}(\xi) + F_{elst}(\xi) + F_{exch}(\xi) + F_{ind}(\xi) + F_{disp}(\xi)\, d\xi$$
$$= w_{strain} + w_{elst} + w_{exch} + w_{ind} + w_{disp} \tag{7}$$

DOI: 10.1021/acs.jpca.9b06865
J. Phys. Chem. A 2019, 123, 7881−7891

This decomposition of the reaction work is a useful tool for summarizing the total contribution to a given region of the reaction.

3. COMPUTATIONAL DETAILS

All geometries have been fully optimized using density functional theory with the M06-2X density functional[109] in the PSI4 ab initio quantum chemistry package.[110,111] The 6-311++G(d,p) basis set[112] was used for all atoms except Br where the def2-TZVPP basis set[113] was used. The local minima and saddle points along the potential energy surface were confirmed using frequency calculations. Reactants and products were confirmed to have positive definite Hessian matrices, whereas transition states only have a single imaginary frequency. The minimum energy path from reactants to products was determined using the stabilized Euler intrinsic reaction coordinate procedure of Morokuma et al.[114] The energy/force profiles, as well as structural and electronic properties were determined from single-point energy calculations on the optimized geometries obtained from the IRC procedure. All symmetry-adapted perturbation theory calculations were performed using the 6-311++G(d,p) basis set in PSI4 at the SAPT0 level. The reaction force and reaction works are all calculated using PYREX,[115] an open-source toolkit for reaction force analysis developed in our research group, which takes energy properties along a reaction coordinate and calculates the necessary numerical derivatives and integrals using functions available in NumPy.[116]

4. RESULTS AND DISCUSSION

4.1. Reaction Mechanism and Energies. In this work, we have addressed the gas-phase formation of hemiacetals from methanol and different substituted aldehydes. Figure 3

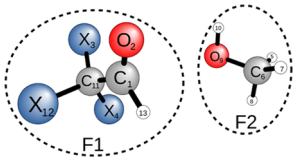

Figure 3. Schematic representation of the reactant complex involved in the hemiacetal formation reaction between the aldehyde CX_3CHO and CH_3OH. This highlights the atomic numbering scheme used in the text. The fragmentation scheme for the complex for SAPT calculations is also shown, where the two fragments are F1 and F2, respectively.

details the atomic numbering scheme used throughout the text; the four unique aldehydes result in four different reactions to study. The reactant, transition state (TS), and product structures for each reaction are detailed in Figure 4. **R1** involves methanol and acetaldehyde, whereas **R2**, **R3**, and **R4** involve fluoral, chloral, and bromal, respectively. The reaction involves the approach of the aldehyde and methanol resulting in shortening of the C_1-O_9 distance. This distance is significantly affected by the halogenation of the aldehydes. **R1** has a C_1-O_9 distance of 2.79 Å. This bond length is notably reduced to 2.53 Å in **R2**. More modest differences are seen in **R3** and **R4** with C_1-O_9 distances of 2.63 and 2.76 Å, respectively. The transition-state complex is characterized by a four-member ring-like structure formed between C_1, O_2, O_9, and H_{10}. In a concerted fashion oxygen addition occurs, forming a new bond between C_1 and O_9, whereas the proton

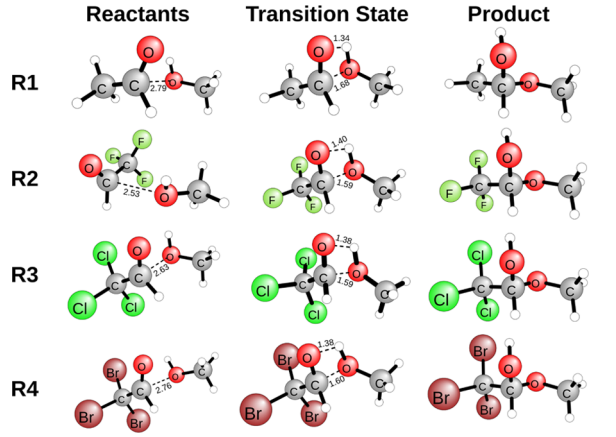

Figure 4. Reactant, transition state, and product structures optimized at the M06-2X/6-311++G(d,p) level for all reactions between methanol (CH_3OH) and an aldehyde of the form CX_3CHO where X = H, F, Cl, and Br. Each reaction has been given a unique identifier as **R1**, **R2**, **R3**, and **R4** for the reactions involving H, F, Cl, and Br, respectively.

(H_{10}) is transferred from O_9 to O_2, forming the final hemiacetal. There is a small difference in the C_1 and O_9 distance in the TS structure between the different reactions. For **R1**, this distance is 1.68 Å and reduces to approximately 1.60 Å in **R2**, **R3**, and **R4**.

The minimum energy pathways determined by the intrinsic reaction coordinate calculation are shown in Figure 5a. From

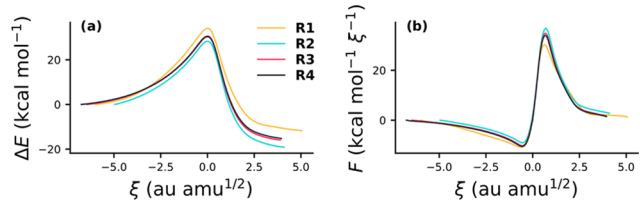

Figure 5. (a) Energy and (b) reaction force profiles for the hemiacetal formation reactions. The IRC was determined at the M06-2X/6-311++G(d,p) level of theory.

the energy plot, it is clear that all reactions are exothermic in nature and that **R2**, **R3**, and **R4** are energetically favorable to **R1**. The activation energy barriers ($\Delta E^{\ddagger}$) for each reaction are reported in Table 1. **R1** has the largest activation energy at 34.05 kcal/mol, whereas **R2** has the lowest activation energy at 28.25 kcal/mol. Meanwhile, **R3** and **R4** have activation energy barriers that are 3.84 and 3.55 kcal/mol lower than that of **R1**, respectively. Some insight into the difference in barrier heights can be obtained by investigating the molecular electrostatic potential (MEP) of the isolated aldehydes. Figure 6 shows the MEP plots for all of the isolated aldehydes. The most significant effect of substituting the hydrogen with a halogen atom is shown in the decrease of the negative region associated with carbonyl oxygen. This is clearly indicative of the electron-withdrawing effect of the halogenated substituents. This decrease in the negative region associated with the carbonyl oxygen increases the relative nucleophilicity of the carbonyl carbon. This argument was made previously by Azofra et al. to rationalize the difference in activation energy barriers between these reactions. To obtain a more detailed analysis on the energy barriers, we perform the reaction force analysis

DOI: 10.1021/acs.jpca.9b06865
J. Phys. Chem. A 2019, 123, 7881−7891

Table 1. Reaction Energy (ΔE^0), Activation Energy ($\Delta E^{\ddagger}$), and Associated Reaction Works (w) for Each Reaction Reported in kcal/mol[a]

	ΔE^0	$\Delta E^{\ddagger}$	w_1	w_2	w_1^{strain}	w_1^{int}	w_2^{strain}	w_2^{int}
R1	−11.77	34.05	28.54(84%)	5.51(16%)	20.12	8.42	29.31	−23.80
R2	−19.15	28.25	24.07(85%)	4.18(15%)	28.11	−4.04	25.68	−21.50
R3	−15.94	30.21	26.04(86%)	4.17(14%)	29.46	−3.43	26.14	−21.97
R4	−15.19	30.50	26.30(86%)	4.20(14%)	29.09	−2.80	26.28	−22.07

[a]Intrinsic reaction coordinate for the data was obtained at the M06-2X/6-311++G(d,p) level of theory. Interaction works are calculated at the SAPT0/6-311++G(d,p) level.

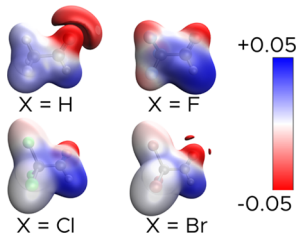

Figure 6. Molecular electrostatic potential at ±0.05 a.u. isosurfaces. The red and blue regions are associated with negative and positive regions, respectively.

4.2. Reaction Force Analysis. The reaction force profiles of all four reactions are plotted in Figure 5b. The essential points along the intrinsic reaction coordinate of each reaction are the critical points of the reaction force profile that correspond to inflection points on the energy profile. The location of the critical points (ξ_{min} and ξ_{max}) and the regions they define are given in Table 2. For each process occurring in each region, there is an associated work value. These are reported for each reaction in Table 1. Considering the fact that the activation energy barrier can be expressed as $\Delta E^{\ddagger} = w_1 + w_2$, we can interpret the work done in each of the first two regions as unique contributions to the total activation energy barrier. With this in mind, it is clear that for each reaction, w_1 accounts for roughly 80% of the activation barrier whereas w_2 accounts for roughly 20%. Comparing the different reactions, note that **R2**, **R3**, and **R4** have lower structural (w_1) and electronic (w_2) work than **R1**. Thus, it will be necessary to investigate both regions to fully explain the difference in the barrier heights. Starting with region 1, **R1** has total work of 28.54 kcal/mol in this region. By contrast, **R2** has total reaction work of 24.07 kcal/mol in region 1. The reaction works for **R3** and **R4** are almost identical with values of 26.04 and 26.30 kcal/mol, respectively. The major chemical event in region 1 is the shortening of the C_1-O_9 distance and the elongation of the O_9-H_{10} bond. The fact that the total work done in this region is smaller in the case of the halogenated aldehydes suggests that the approach of the reactants is more energetically favorable in those cases. Indeed, the MEPs shown in Figure 6 suggest that this should be the case, due to the electron-withdrawing effect of the halogens increasing the nucleophilicity at the carbonyl carbon. In region 2, **R1** again has the largest total work value with w_2 = 5.51 kcal/mol. The reactions involving halogenated aldehydes are significantly lower with w_2 = 4.18 and 4.17 kcal/mol for **R2** and **R3**, respectively, whereas **R4** is only slightly higher at 4.20 kcal/mol. This indicates that the electronic reordering is more favorable in the case of the halogenated aldehydes. The differences here are more subtle and will be analyzed in greater detail in the next section.

Table 2. Critical Points of the Reaction Energy Profile Corresponding to the Reactant (ξ_R) and Product (ξ_P) Structures and Critical Points of the Reaction Force Corresponding to the Force Minimum (ξ_{min}) and Maximum (ξ_{max})[a]

	ξ_R	ξ_{min}	ξ_{max}	ξ_P
R1	−6.00	−0.65	0.65	5.05
R2	−4.95	−0.55	0.70	4.10
R3	−6.45	−0.55	0.70	3.90
R4	−6.75	−0.55	0.65	3.95

[a]All values are in units of amu$^{1/2}$ bohr, relative to their respective transition-state structure located at ξ_{TS} = 0.00 amu$^{1/2}$ bohr.

4.3. SAPT Decomposition of Reaction Force and Reaction Work. Further insight into the contributions to the activation energy barrier can be obtained using SAPT decomposition of the reaction force. This analysis requires careful partitioning of the reactants into distinct fragments. For the purpose of this reaction, we partition the reactants such that fragment 1 (F1) consists of the aldehyde whereas the interacting methanol is fragment 2 (F2). This partitioning scheme is shown visually in Figure 3. To investigate the substituent effect of halogenation of the aldehyde on the reaction, we will calculate the difference in the reaction work (Δw) for **R2**, **R3**, and **R4** relative to **R1**.

$$\Delta w = w(CX_3) - w(CH_3) \tag{8}$$

This difference between the reaction works is directly related to the difference in activation energy between the two reactions. Recall that the reactions works can be related to the activation energy via eq 2. We can express the difference in activation energies in the following way

$$\begin{aligned}\Delta E &= \Delta E^{\ddagger}(CX_3) - \Delta E^{\ddagger}(CH_3)\\ &= [w_1(CX_3) + w_2(CX_3)] - [w_1(CH_3) + w_2(CH_3)]\\ &= [w_1(CX_3) - w_1(CH_3)] + [w_2(CX_3) - w_2(CH_3)]\\ &= \Delta w_1 + \Delta w_2\end{aligned} \tag{9}$$

Making use of the SAPT decomposition of the reaction work from eq 7 it is possible to characterize this substituent effect in terms of differences in electrostatic, exchange, induction, and dispersion interactions for each region of the reaction coordinate.

Figure 7 depicts the differences in the reaction interaction works for hemiacetal formation involving halogenated aldehydes. The most immediately striking feature in the plot is the disparity between the work difference in region 1 compared with region 2. This result clearly shows that any difference in the lower activation energy barrier is primarily a

DOI: 10.1021/acs.jpca.9b06865
J. Phys. Chem. A 2019, 123, 7881−7891

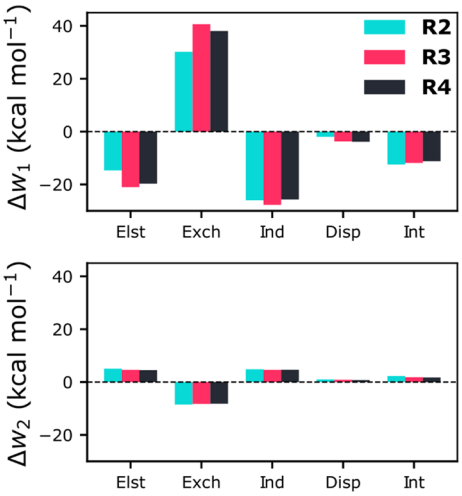

Figure 7. Difference in reaction work (Δw) for region 1 (Δw_1) and region 2 (Δw_2) for **R2** (X = F), **R3** (X = Cl), **R4** (X = Br).

result of interactions in region 1 rather than those in the transition-state region. This further implies that the substituent effect is most significant during the structural rearrangement than the the electronic reorganization.

Focusing on Δw_1, it is clear that the substituent effect is largely driven by more favorable electrostatic and induction interactions between the two monomers. The more electronegative halogens result in more favorable electrostatic interactions with Δw_1 contributions of −14.7, −21.0, and −19.7 kcal mol^{-1} for **R2**, **R3**, and **R4**, respectively. Due to the increase in the number of electrons, there is a significantly more unfavorable exchange interaction with differences of 30.2, 40.6, and 38.1 kcal mol^{-1} for **R2**, **R3**, and **R4**, respectively. The more favorable induction is comparable amongst the three reactions with Δw_1 contributions of approximately 27.0 kcal mol^{-1}. The effect of dispersion is small but certainly non-negligible with dispersion contributions of −2.0, −3.7, and −3.9 kcal mol^{-1} for **R2**, **R3**, and **R4**, respectively.

When considering Δw_2, it is interesting to note that the halogenated reactions have slighlty less favorable interactions in this region, with total interaction contributions of +2.3, +1.8, and +1.7 kcal mol^{-1} for **R2**, **R3**, and **R4**, respectively. Interestingly, all of the reactions have an exchange interaction energy that is more favorable by about 8.0 kcal mol^{-1}. This is indicative of the electron-withdrawing effect of the halogens. With less electron density associated with the COH group of the aldehyde there is less exchange repulsion during the electronic reorganization of the reaction.

From the SAPT data, we can conclude that the substituent effect is largely a result of more favorable electrostatic, induction, and dispersion interactions that occur prior to the transition-state region. However, this insight does not address an important distinction: is this substituent effect a result of direct interactions of the CX_3 substituent with the menthanol monomer, or is it primarily an indirect effect resulting from the withdrawing of electron density away from the COH substituent? This is a point that can be explored by considering the interactions of different functional groups, a point we will address fully in the next section.

One final point to address concerns the validity/accuracy of SAPT reaction forces. It has been well documented in the literature that interaction energies calculated using SAPT can run into difficulties at a short range where bonds are being broken/formed and the approximation of intermolecular interactions being treated as a perturbation breaks down. As a point of comparison, Figure S1 in the Supporting Information shows SAPT0 results for the interaction component of the reaction force (F_{int}) of **R1** and **R2** with data from supermolecular calculations at the MP2/6-311++G(d,p) level. As expected, there are significant differences between the total reaction forces at short internuclear distances. Tables S1 and S2 compare the relative reaction forces between the two reactions calculated at the MP2 and SAPT0 levels. The average difference between the relative reaction forces is less than 1 kcal mol^{-1}. Considering this result, it is important to highlight that this approach will be very useful for relative energy differences, like the relative reaction works (Δw) calculated in this study. However, more care will be needed for accurate total reaction forces. This is a point that is outside the scope of this current study but will be explored in more detail in future studies.

4.4. F-SAPT Decomposition of Reaction Force and Work. Here, we will explore the use of the functional group partition of symmetry-adapted perturbation theory (F-SAPT) within the context of reaction force analysis. Within this context, the SAPT partitioning of the complex into two monomers is viewed as "order-1" partitioning of the system. F-SAPT seeks to decompose the interaction energy terms (E^{term}) into an "order-2" partitioning scheme in which the interaction between functional groups a and b on monomers A and B, respectively, is captured in an energy term E_{ab}^{term}. This is done in an exact way such that the original order-1 interaction term is recovered when summing over all order-2 interactions

$$E^{term} = \sum_{ab} E_{ab}^{term} \tag{10}$$

The theoretical details behind F-SAPT are nontrivial and require a careful mathematical treatment of the SAPT expressions. For a more rigorous explanation of the theory, the reader is directed to the relevant literature.[74,75] For our purposes, we will use the result from eq 10 and define functional group contributions to the reaction force. Taking the negative energy gradient of the interaction term allows us to consider functional group contributions to the reaction force

$$F^{term} = -\frac{\partial E^{term}}{\partial \xi} = -\sum_{ab} \frac{\partial E_{ab}^{term}}{\partial \xi}$$

$$F^{term} = \sum_{ab} F_{ab}^{term} \tag{11}$$

Integrating over the force will also yield functional group partitioning for the reaction work as well such that

$$w^{term} = \sum_{ab} w_{ab}^{term} \tag{12}$$

In preparation of the F-SAPT calculations, we employ the partitioning scheme shown in Figure 8. Essentially, the aldehyde can be partitioned into the CX_3 substituent and the COH carbonyl group whereas methanol can be partitioned into the methyl CH_3 group and the hydroxyl OH group. The σ-bonds associated with connecting the functional group fragments are treated as a "linker". This linker can be assigned to each functional group in a 50−50 fashion or assigned by charge. For this analysis, we have chosen the latter. However, it

DOI: 10.1021/acs.jpca.9b06865
J. Phys. Chem. A 2019, 123, 7881−7891

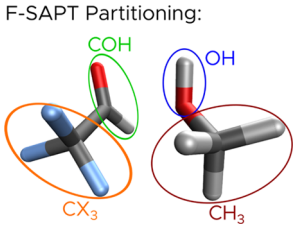

Figure 8. Functional group partitioning scheme used for the hemiacetal formation reaction between the aldehyde CX_3CHO and CH_3OH.

should be noted that both charge-partitioning methods have been shown to produce essentially equivalent results when the chosen fragments are linked with a simple σ bond.[75] It should be noted that as functional groups are distorted, this functional group picture may break down. It is imperative that fragments are chosen carefully for a given region of the reaction coordinate. Within regions 1 and 2 of the current reactions, the O_9-H_{10} bond length stretches and the C_1-O_2 bond distorts as well but does not completely break down this functional group partitioning.

Let us consider the earlier correlation of the barrier heights with the negative electron density associated with the carbonyl. Implicit in this explanation is that the substituent effect is indirect in nature, i.e., the substituent is drawing electron density away from the acetyl group and thus facilitating a more favorable interaction between the acetyl group and the hydroxy group of methanol. We are able to specifically investigate this effect using F-SAPT, and within the framework of reaction force analysis we can quantify its contribution to the overall activation energy barrier. To further investigate the substituent effects, we will investigate the same relative works (Δw) explored in the previous section. However, now, each individual work term can be broken down into functional group interactions

$$\Delta w_{ab} = w_{ab}(CX_3) - w_{ab}(CH_3) \quad (13)$$

Using this approach, if the indirect substituent effect is the primary interaction, then **R2**, **R3**, and **R4** should show a much more favorable COH−OH interaction throughout the reaction.

Figure 9 shows the F-SAPT decomposition of the work for the two primary interactions in the reaction, the CX_3−OH and COH−OH interactions. Starting with the COH−OH interaction, it is clear that in region 1 all reactions with halogenated aldehydes benefit from more favorable electrostatic, induction, and dispersion interactions. However, these more favorable interactions are counteracted by a significant increase in the exchange repulsion between the two fragments, leading to a total interaction that is only marginally favorable. The total Δw_1 for the COH−OH interaction is −3.30, −2.73, and −3.06 for **R2**, **R3**, and **R4**, respectively. Moving on to region 2, due to the electron-withdrawing effect of the CX_3 substituents, there is less electron density associated with the COH fragment, resulting in lower exchange interaction for this region. However, this also results in less favorable electrostatic and induction interactions, leading to total works that are less favorable. In fact, they are large enough in magnitude to nearly cancel out the favorable interaction in region 1 with total Δw_2 values of 2.91, 2.30, and 2.09 kcal/mol for **R2**, **R3**, and **R4**, respectively.

The CX_3−OH interactions similarly have more favorable electrostatic and induction energy in region 1. However, given the distance between them there is less exchange repulsion between these two fragments, leading to much more favorable interaction throughout the region, with total Δw_1 values of −8.78, −9.59, and −8.75 kcal/mol for **R2**, **R3**, and **R4**, respectively. Unlike the the COH−OH interactions, there are no unfavorable interactions in region 2 that counterbalance these favorable interactions in region 1. That being said, we can conclude that the primary substituent effect that leads to a lowering of the activation energy barrier for substituted aldehydes in the formation of hemiacetals is the noncovalent interaction between the CX_3 substituent of the aldehyde and the OH group on methanol.

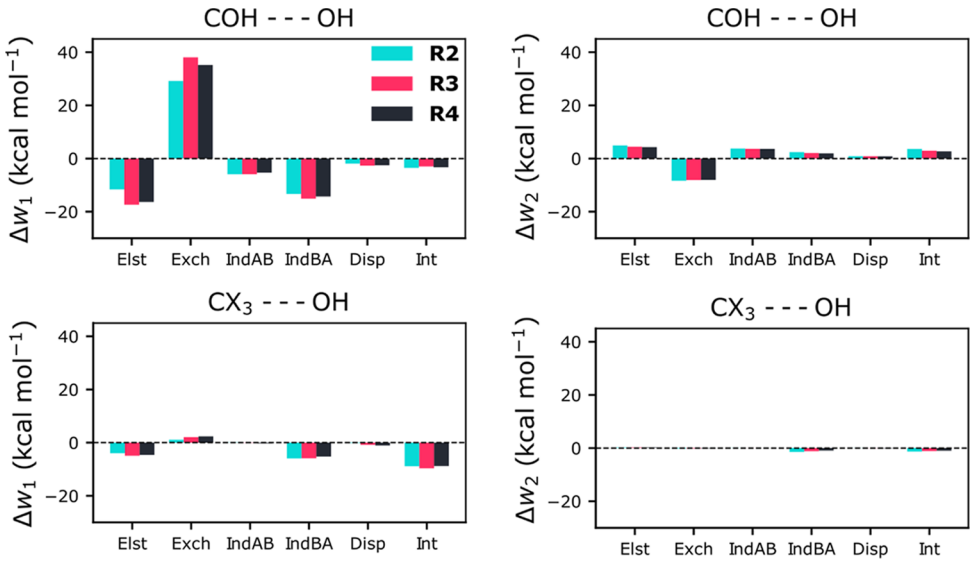

Figure 9. Difference in reaction work (Δw) for region 1 (Δw_1) and region 2 (Δw_2) for the interactions between COH−OH and CX_3−OH. The differences of the interactions on the CH_3 group on methanol were minimal and thus are not shown here.

DOI: 10.1021/acs.jpca.9b06865
J. Phys. Chem. A 2019, 123, 7881−7891

5. CONCLUSIONS

In this work, we have developed a new approach to reaction force analysis that utilizes symmetry-adapted perturbation theory (SAPT) and its functional group partition (F-SAPT) to decompose the reaction force into unique chemically relevant energy contributions. One of the main goals of this work was to introduce the approach of using SAPT and F-SAPT for reaction force analysis. The application highlights the potential for this method to provide new insight into the interactions that drive chemical reactions. In the hemiacetal formation reactions considered in this work, the activation energy barrier is significantly reduced in the case of the halogenated aldehydes (X = F, Cl, or Br) when compared with the reaction involving acetaldehyde (X = H). Reaction force analysis shows that the difference in the activation energy barrier is primarily due to energy differences that occur prior to the transition-state region. Our SAPT analysis provides further insight and details that the reactions involving halogenated aldehydes benefit primarily from more favorable electrostatic and induction interactions. Using F-SAPT, we were able to show that this favorable interaction is a result of direct interaction of the CX_3 group with the OH on methanol rather than an indirect consequence of the electron-withdrawing effect the CX_3 group has on the COH group of the aldehyde, as has been suggested previously in the literature.

One advantage of perturbative approaches like SAPT is the ability to systematically treat higher order interactions. Certain reaction mechanisms may require a higher level SAPT treatment, and with each higher-order effect having its own term in the perturbative series, these effects can be investigated in a systematic way. Additionally, SAPT also has an intramolecular variant[117] (I-SAPT), which makes this approach readily able to study unimolecular rearrangements. These efforts are underway in our group and will be later expanded on in detail. In summary, SAPT is a very useful/intuitive choice for decomposition of the reaction force opening up new possibilities for studying chemical reaction mechanisms.

■ ASSOCIATED CONTENT

Supporting Information

The Supporting Information is available free of charge on the ACS Publications website at DOI: 10.1021/acs.jpca.9b06865.

Transition-state structures for all reactions provided as xyz files (ZIP)

Comparison of SAPT results with supermolecular MP2 calculations (PDF)

■ AUTHOR INFORMATION

Corresponding Author

*E-mail: wallace.derricotte@morehouse.edu.

ORCID

Wallace D. Derricotte: 0000-0001-5709-5168

Notes

The author declares no competing financial interest.

■ ACKNOWLEDGMENTS

This work is supported by the National Science Foundation Research Initiation Award under award number 1900710, as well as start-up funds provided by Morehouse College. The content presented in this publication is solely the responsibility of the authors and does not necessarily represent the official views of the National Science Foundation. The author would also like to thank Steven Wheeler and C. David Sherrill for valuable feedback throughout the preparation of this manuscript.

■ REFERENCES

(1) Kolb, G. *Multiphase Catalytic Reactors*; John Wiley & Sons, Ltd, 2016; pp 330−364.

(2) Dudukovi, M. P.; Larachi, F.; Mills, P. L. Multiphase Catalytic Reactors: A Perspective on Current Knowledge and Future Trends. *Catal. Rev.* **2002**, *44*, 123−246.

(3) Halpin, D. R.; Harbury, P. B. DNA Display II. Genetic Manipulation of Combinatorial Chemistry Libraries for Small-Molecule Evolution. *PLoS Biol.* **2004**, *2*, e174.

(4) Shi, J.; Tang, C. W. Anthracene Derivatives for Stable Blue-Emitting Organic Electroluminescence Devices. *Appl. Phys. Lett.* **2002**, *80*, 3201−3203.

(5) Poizot, P.; Laruelle, S.; Grugeon, S.; Dupont, L.; Tarascon, J.-M. Nano-Sized Transition-Metal Oxides as Negative-Electrode Materials for Lithium-Ion Batteries. *Nature* **2000**, *407*, 496.

(6) Zhang, Q.; Tsang, D.; Kuwabara, H.; Hatae, Y.; Li, B.; Takahashi, T.; Lee, S. Y.; Yasuda, T.; Adachi, C. Nearly 100% Internal Quantum Efficiency in Undoped Electroluminescent Devices Employing Pure Organic Emitters. *Adv. Mater.* **2015**, *27*, 2096−2100.

(7) Yang, H.; Zhuang, G. V.; Ross, P. N. Thermal Stability of $LiPF_6$ Salt and Li-Ion Battery Electrolytes Containing $LiPF_6$. *J. Power Sources* **2006**, *161*, 573−579.

(8) Marcus, R. A. Electrostatic Free Energy and Other Properties of States Having Nonequilibrium Polarization. I. *J. Chem. Phys.* **1956**, *24*, 979−989.

(9) Cooper, D. L.; Gerratt, J.; Raimondi, M. *Advances in Chemical Physics*; John Wiley & Sons, Ltd, 2007; pp 319−397.

(10) Fukui, K. Role of Frontier Orbitals in Chemical Reactions. *Science* **1982**, *218*, 747−754.

(11) England, W.; Salmon, L. S.; Ruedenberg, K. Localized Molecular Orbitals: A Bridge Between Chemical Intuition and Molecular Quantum Mechanics. *Mol. Orbitals* **1971**, 31−123.

(12) Saha, S.; Roy, R. K.; Ayers, P. W. Are the Hirshfeld and Mulliken Population Analysis Schemes Consistent with Chemical Intuition? *Int. J. Quantum Chem.* **2009**, *109*, 1790−1806.

(13) Deringer, V. L.; Pan, F.; George, J.; Müller, P.; Dronskowski, R.; Englert, U. Intermolecular Contacts in Bromomalonic Aldehyde-Intuition, Experiment, and Theory. *CrystEngComm* **2014**, *16*, 135−138.

(14) Fukui, K. The Path of Chemical Reactions - The IRC Approach. *Acc. Chem. Res.* **1981**, *14*, 363−368.

(15) Toro-Labbé, A.; Gutiérrez-Oliva, S.; Murray, J. S.; Politzer, P. The Reaction Force and the Transition Region of a Reaction. *J. Mol. Model.* **2009**, *15*, 707−710.

(16) Politzer, P.; Toro-Labbé, A.; Gutiérrez-Oliva, S.; Herrera, B.; Jaque, P.; Concha, M. C.; Murray, J. S. The Reaction Force: Three Key Points Along an Intrinsic Reaction Coordinate. *J. Chem. Sci.* **2005**, *117*, 467−472.

(17) Martínez, J.; Toro-Labbé, A. The Reaction Force. A Scalar Property to Characterize Reaction Mechanisms. *J. Math. Chem.* **2009**, *45*, 911−927.

(18) Toro-Labbé, A.; Gutiérrez-Oliva, S.; Murray, J. S.; Politzer, P. A New Perspective on Chemical and Physical Processes: The Reaction Force. *Mol. Phys.* **2007**, *105*, 2619−2625.

(19) Jaque, P.; Toro-Labbé, A.; Politzer, P.; Geerlings, P. Reaction Force Constant and Projected Force Constants of Vibrational Modes Along the Path of an Intramolecular Proton Transfer Reaction. *Chem. Phys. Lett.* **2008**, *456*, 135−140.

(20) Yepes, D.; Donoso-Tauda, O.; Pèrez, P.; Murray, J. S.; Politzer, P.; Jaque, P. The Reaction Force Constant as an Indicator of Synchronicity/Nonsynchronicity in [4+2] Cycloaddition Processes. *Phys. Chem. Chem. Phys.* **2013**, *15*, 7311−7320.

DOI: 10.1021/acs.jpca.9b06865
J. Phys. Chem. A 2019, 123, 7881−7891

(21) Echegaray, E.; Toro-Labbé, A. Reaction Electronic Flux: A New Concept To Get Insights into Reaction Mechanisms. Study of Model Symmetric Nucleophilic Substitutions. *J. Phys. Chem. A* **2008**, *112*, 11801−11807.
(22) Flores-Morales, P.; Gutiérrez-Oliva, S.; Silva, E.; Toro-Labbé, A. The Reaction Electronic Flux: A New Descriptor of the Electronic Activity Taking Place During a Chemical Reaction. Application to the Characterization of the Mechanism of the Schiff's Base Formation in the Maillard Reaction. *J. Mol. Struct.: THEOCHEM* **2010**, *943*, 121−126.
(23) Morell, C.; Tognetti, V.; Bignon, E.; Dumont, E.; Hernandez-Haro, N.; Herrera, B.; Grand, A.; Gutiérrez-Oliva, S.; Joubert, L.; Toro-Labbé, A.; Chermette, H. Insights into the Chemical Meanings of the Reaction Electronic Flux. *Theor. Chem. Acc.* **2015**, *134*, 133.
(24) Martínez-Araya, J. I.; Toro-Labbé, A. Reaction Electronic Flux as a Fluctuation of Relative Interatomic Electronic Populations. *J. Phys. Chem. C* **2015**, *119*, 3040−3049.
(25) Vogt-Geisse, S.; Toro-Labbé, A. The Mechanism of the Interstellar Isomerization Reaction $HOC^+ \rightarrow HCO^+$ Catalyzed by H_2: New Insights from the Reaction Electronic Flux. *J. Chem. Phys.* **2009**, *130*, No. 244308.
(26) Cern, M. L.; Herrera, B.; Araya, P.; Gracia, F.; Toro-Labbé, A. The Mechanism of Methanol Decomposition by CuO. A Theoretical Study Based on the Reaction Force and Reaction Electronic Flux Analysis. *J. Mol. Model.* **2011**, *17*, 1625−1633.
(27) Giri, S.; Echegaray, E.; Ayers, P. W.; Nuñez, A. S.; Lund, F.; Toro-Labbé, A. Insights into the Mechanism of an SN2 Reaction from the Reaction Force and the Reaction Electronic Flux. *J. Phys. Chem. A* **2012**, *116*, 10015−10026.
(28) Inostroza-Rivera, R.; Herrera, B.; Toro-Labbé, A. Using the Reaction Force and the Reaction Electronic Flux on the Proton Transfer of Formamide Derived Systems. *Phys. Chem. Chem. Phys.* **2014**, *16*, 14489−14495.
(29) Giri, S.; Inostroza-Rivera, R.; Herrera, B.; Núñez, A. S.; Lund, F.; Toro-Labbé, A. The Mechanism of Menshutkin Reaction in Gas and Solvent Phases from the Perspective of Reaction Electronic Flux. *J. Mol. Model.* **2014**, *20*, 2353.
(30) Cortés-Arriagada, D.; Gutiérrez-Oliva, S.; Herrera, B.; Soto, K.; Toro-Labbé, A. The Mechanism of Chemisorption of Hydrogen Atom on Graphene: Insights from the Reaction Force and Reaction Electronic Flux. *J. Chem. Phys.* **2014**, *141*, No. 134701.
(31) Lamsabhi, A. M.; Gutiérrez-Oliva, S.; Mó, O.; Toro-Labbé, A.; Yáñez, M. Effects of the Ionization in the Tautomerism of Uracil: A Reaction Electronic Flux Perspective. *J. Comput. Chem.* **2015**, *36*, 2135−2145.
(32) Durán, R.; Vöhringer-Martinez, E.; Toro-Labbé, A.; Herrera, B. Reaction Electronic Flux and its Role in DNA Intramolecular Proton Transfers. *J. Mol. Model.* **2016**, *22*, 145.
(33) Vogt-Geisse, S.; Toro-Labbé, A. Chemical Potential and Reaction Electronic Flux in Symmetry Controlled Reactions. *J. Comput. Chem.* **2016**, *37*, 1794−1800.
(34) Villegas-Escobar, N.; Vogt-Geisse, S.; Gutiérrez-Oliva, S.; Toro-Labbé, A. Symmetry-Adapted Reaction Electronic Flux in Cycloaddition Reactions. *Theor. Chem. Acc.* **2016**, *135*, 191.
(35) Ortega-Moo, C.; Durán, R.; Herrera, B.; Gutiérrez-Oliva, S.; Toro-Labbé, A.; Vargas, R. Study of Antiradical Mechanisms with Dihydroxybenzenes Using Reaction Force and Reaction Electronic Flux. *Phys. Chem. Chem. Phys.* **2017**, *19*, 14512−14519.
(36) Matute, R. A.; Pérez, P.; Chamorro, E.; Villegas-Escobar, N.; Cortés-Arriagada, D.; Herrera, B.; Gutiérrez-Oliva, S.; Toro-Labbé, A. Reaction Electronic Flux Perspective on the Mechanism of the Zimmerman Di-p-methane Rearrangement. *J. Org. Chem.* **2018**, *83*, 5969−5974.
(37) Guzmán-Angel, D.; Gutiérrez-Oliva, S.; Toro-Labbé, A. Hydrogenation and Hydration of Carbon Dioxide: A Detailed Characterization of the Reaction Mechanisms Based on the Reaction Force and Reaction Electronic Flux Analyses. *J. Mol. Model.* **2019**, *25*, 16.
(38) Aazaad, B.; Mano Priya, A.; Senthilkumar, L. Addition and Abstraction Reaction Mechanism of 2,4,5-Trimethylphenol with OH Radical - A First Principle Study. *Comput. Theor. Chem.* **2016**, *1092*, 90−107.
(39) Aazaad, B.; Lakshmipathi, S. Reaction of NO_3 Radical with Benzyl Alcohol - A DFT Study. *Comput. Theor. Chem.* **2017**, *1102*, 51−59.
(40) Priya, A. M.; Lakshmipathi, S. Atmospheric fate of diketones and OH radical-kinetics, reaction force, ETS-NOCV analysis. *Mol. Phys.* **2017**, *115*, 839−859.
(41) Yepes, D.; Murray, J. S.; Pèrez, P.; Domingo, L. R.; Politzer, P.; Jaque, P. Complementarity of Reaction Force and Electron Localization Function Analyses of Asynchronicity in Bond Formation in Diels-Alder Reactions. *Phys. Chem. Chem. Phys.* **2014**, *16*, 6726−6734.
(42) Esquivel, R. O.; Molina-Espíritu, M.; Dehesa, J. S.; Angulo, J. C.; Antolín, J. Concurrent Phenomena at the Transition Region of Selected Elementary Chemical Reactions: An Information-Theoretical Complexity Analysis. *Int. J. Quantum Chem.* **2012**, *112*, 3578−3586.
(43) Murray, J. S.; Lane, P.; Nieder, A.; Klapötke, T. M.; Politzer, P. Enhanced Detonation Sensitivities of Silicon Analogs of PETN: Reaction Force Analysis and the Role of σ-hole Interactions. *Theor. Chem. Acc.* **2010**, *127*, 345−354.
(44) Murray, J. S.; Lane, P.; Göbel, M.; Klapötke, T. M.; Politzer, P. Reaction Force Analyses of Nitro-aci Tautomerizations of Trinitromethane, the Elusive Trinitromethanol, Picric Acid and 2,4-dinitro-1H-imidazole. *Theor. Chem. Acc.* **2009**, *124*, 355.
(45) Morokuma, K. Molecular Orbital Studies of Hydrogen Bonds. III. C═O...H-O Hydrogen Bond in $H_2CO...H_2O$ and $H_2CO_2...H_2O$. *J. Chem. Phys.* **1971**, *55*, 1236−1244.
(46) Joshi, B. D.; Morokuma, K. Force Decomposition Analysis Along Reaction Coordinate. *J. Chem. Phys.* **1977**, *67*, 4880−4883.
(47) van Zeist, W.-J.; Bickelhaupt, F. M. The Activation Strain Model of Chemical Reactivity. *Org. Biomol. Chem.* **2010**, *8*, 3118−3127.
(48) Fernández, I.; Bickelhaupt, F. M. The Activation Strain Model and Molecular Orbital Theory: Understanding and Designing Chemical Reactions. *Chem. Soc. Rev.* **2014**, *43*, 4953−4967.
(49) Ess, D. H.; Houk, K. N. Distortion/Interaction Energy Control of 1,3-Dipolar Cycloaddition Reactivity. *J. Am. Chem. Soc.* **2007**, *129*, 10646−10647.
(50) Bickelhaupt, F. M.; Houk, K. N. Analyzing Reaction Rates with the Distortion/Interaction-Activation Strain Model. *Angew. Chem., Int. Ed.* **2017**, *56*, 10070−10086.
(51) Kitaura, K.; Morokuma, K. A New Energy Decomposition Scheme for Molecular Interactions Within the Hartree-Fock Approximation. *Int. J. Quantum Chem.* **1976**, *10*, 325−340.
(52) van Bochove, M. A.; Swart, M.; Bickelhaupt, F. M. Nucleophilic Substitution at Phosphorus (SN2@P): Disappearance and Reappearance of Reaction Barriers. *J. Am. Chem. Soc.* **2006**, *128*, 10738−10744.
(53) Laloo, J. Z. A.; Rhyman, L.; Larrañaga, O.; Ramasami, P.; Bickelhaupt, F. M.; de Cózar, A. Ion-Pair SN2 Reaction of OH- and CH3Cl: Activation Strain Analyses of Counterion and Solvent Effects. *Chem. Asian J.* **2018**, *13*, 1138−1147.
(54) Kubelka, J.; Bickelhaupt, F. M. Activation Strain Analysis of SN2 Reactions at C, N, O, and F Centers. *J. Phys. Chem. A* **2017**, *121*, 885−891.
(55) de Jong, G. T.; Bickelhaupt, F. M. Transition-State Energy and Position along the Reaction Coordinate in an Extended Activation Strain Model. *ChemPhysChem* **2007**, *8*, 1170−1181.
(56) de Jong, G. T.; Bickelhaupt, F. M. Catalytic Carbon-Halogen Bond Activation: Trends in Reactivity, Selectivity, and Solvation. *J. Chem. Theory Comput.* **2007**, *3*, 514−529.
(57) Fernández, I.; Solà, M.; Bickelhaupt, F. M. Why Do Cycloaddition Reactions Involving C60 Prefer [6,6] over [5,6] Bonds? *Chem. − Eur. J.* **2013**, *19*, 7416−7422.
(58) Xu, L.; Doubleday, C. E.; Houk, K. N. Dynamics of 1,3-Dipolar Cycloaddition Reactions of Diazonium Betaines to Acetylene and Ethylene: Bending Vibrations Facilitate Reaction. *Angew. Chem., Int. Ed.* **2009**, *48*, 2746−2748.

DOI: 10.1021/acs.jpca.9b06865
J. Phys. Chem. A 2019, 123, 7881−7891

(59) Liu, F.; Paton, R. S.; Kim, S.; Liang, Y.; Houk, K. N. Diels-Alder Reactivities of Strained and Unstrained Cycloalkenes with Normal and Inverse-Electron-Demand Dienes: Activation Barriers and Distortion/Interaction Analysis. *J. Am. Chem. Soc.* **2013**, *135*, 15642−15649.
(60) Fernández, I.; Bickelhaupt, F. M.; Cossío, F. P. Type-I Dyotropic Reactions: Understanding Trends in Barriers. *Chem. − Eur. J.* **2012**, *18*, 12395−12403.
(61) Fernández, I.; Bickelhaupt, F. M.; Cossío, F. P. Ene-ene-yne Reactions: Activation Strain Analysis and the Role of Aromaticity. *Chem. − Eur. J.* **2014**, *20*, 10791−10801.
(62) Ziegler, T.; Rauk, A. On the Calculation of Bonding Energies by the Hartree-Fock-Slater Method. *Theor. Chim. Acta* **1977**, *46*, 1−10.
(63) Ziegler, T.; Rauk, A. A Theoretical Study of the Ethylene-Metal Bond in Complexes Between Copper(1+), Silver(1+), Gold(1+), Platinum(0) or Platinum(2+) and Ethylene, Based on the Hartree-Fock-Slater Transition-State Method. *Inorg. Chem.* **1979**, *18*, 1558−1565.
(64) Ziegler, T.; Rauk, A. Carbon Monoxide, Carbon Monosulfide, Molecular Nitrogen, Phosphorus Trifluoride, and Methyl Isocyanide as σ-Donors and π-Acceptors. A Theoretical Study by the Hartree-Fock-Slater Transition-State Method. *Inorg. Chem.* **1979**, *18*, 1755−1759.
(65) Mitoraj, M.; Michalak, A. Natural Orbitals for Chemical Valence as Descriptors of Chemical Bonding in Transition Metal Complexes. *J. Mol. Model.* **2007**, *13*, 347−355.
(66) Michalak, A.; Mitoraj, M.; Ziegler, T. Bond Orbitals from Chemical Valence Theory. *J. Phys. Chem. A* **2008**, *112*, 1933−1939.
(67) Mitoraj, M. P.; Michalak, A.; Ziegler, T. A Combined Charge and Energy Decomposition Scheme for Bond Analysis. *J. Chem. Theory Comput.* **2009**, *5*, 962−975.
(68) Banerjee, S. Understanding the Ring-Opening, Chelation and Non-Chelation Reactions Between Nedaplatin and Thiosulfate: A DFT Study Based on NBO, ETS-NOCV and QTAIM. *Theor. Chem. Acc.* **2016**, *135*, 20.
(69) Šebesta, F.; Burda, J. V. Interactions of Ascorbic Acid with Satraplatin and its trans Analog JM576: DFT Computational Study. *Eur. J. Inorg. Chem.* **2018**, *2018*, 1481−1491.
(70) Díaz, S.; Brela, M. Z.; Gutiérrez-Oliva, S.; Toro-Labbé, A.; Michalak, A. ETS-NOCV Decomposition of the Reaction Force: The HCN/CNH Isomerization Reaction Assisted by Water. *J. Comput. Chem.* **2017**, *38*, 2076−2087.
(71) Rincón, E.; Jaque, P.; Toro-Labbé, A. Reaction Force Analysis of the Effect of Mg(II) on the 1,3 Intramolecular Hydrogen Transfer in Thymine. *J. Phys. Chem. A* **2006**, *110*, 9478−9485.
(72) Talaga, P.; Brela, M. Z.; Michalak, A. ETS-NOCV Decomposition of the Reaction Force for Double-Proton Transfer in Formamide-Derived Systems. *J. Mol. Model.* **2017**, *24*, 27.
(73) Stone, A. J. *The Theory of Intermolecular Forces*; Clarendon Press, 1997; Google-Books-ID: nQyhXDVnmowC.
(74) Parrish, R. M.; Sherrill, C. D. Spatial Assignment of Symmetry Adapted Perturbation Theory Interaction Energy Components: The Atomic SAPT Partition. *J. Chem. Phys.* **2014**, *141*, No. 044115.
(75) Parrish, R. M.; Parker, T. M.; Sherrill, C. D. Chemical Assignment of Symmetry-Adapted Perturbation Theory Interaction Energy Components: The Functional-Group SAPT Partition. *J. Chem. Theory Comput.* **2014**, *10*, 4417−4431.
(76) Hohenstein, E. G.; Sherrill, C. D. Density Fitting and Cholesky Decomposition Approximations in Symmetry-Adapted Perturbation Theory: Implementation and Application to Probe the Nature of π-π Interactions in Linear Acenes. *J. Chem. Phys.* **2010**, *132*, No. 184111.
(77) Hohenstein, E. G.; Sherrill, C. D. Density Fitting of Intramonomer Correlation Effects in Symmetry-Adapted Perturbation Theory. *J. Chem. Phys.* **2010**, *133*, No. 014101.
(78) Hohenstein, E. G.; Parrish, R. M.; Sherrill, C. D.; Turney, J. M.; Schaefer, H. F. Large-Scale Symmetry-Adapted Perturbation Theory Computations Via Density Fitting and Laplace Transformation Techniques: Investigating the Fundamental Forces of DNA-Intercalator Interactions. *J. Chem. Phys.* **2011**, *135*, No. 174107.
(79) Hohenstein, E. G.; Sherrill, C. D. Efficient Evaluation of Triple Excitations in Symmetry-Adapted Perturbation Theory via Second-Order Møller-Plesset Perturbation Theory Natural Orbitals. *J. Chem. Phys.* **2010**, *133*, No. 104107.
(80) Parrish, R. M.; Hohenstein, E. G.; Sherrill, C. D. Tractability Gains in Symmetry-Adapted Perturbation Theory Including Coupled Double Excitations: CCD+ST(CCD) Dispersion with Natural Orbital Truncations. *J. Chem. Phys.* **2013**, *139*, No. 174102.
(81) Parrish, R. M.; Thompson, K. C.; Martínez, T. J. Large-Scale Functional Group Symmetry-Adapted Perturbation Theory on Graphical Processing Units. *J. Chem. Theory Comput.* **2018**, *14*, 1737−1753.
(82) Parrish, R. M.; Sherrill, C. D. Quantum-Mechanical Evaluation of π-π versus Substituent-π Interactions in π Stacking: Direct Evidence for the Wheeler-Houk Picture. *J. Am. Chem. Soc.* **2014**, *136*, 17386−17389.
(83) Parrish, R. M.; Sitkoff, D. F.; Cheney, D. L.; Sherrill, C. D. The Surprising Importance of Peptide Bond Contacts in Drug-Protein Interactions. *Chem. − Eur. J.* **2017**, *23*, 7887−7890.
(84) Bakr, B. W.; Sherrill, C. D. Analysis of Transition State Stabilization by Non-Covalent Interactions in the Houk-List Model of Organocatalyzed Intermolecular Aldol Additions Using Functional-Group Symmetry-Adapted Perturbation Theory. *Phys. Chem. Chem. Phys.* **2016**, *18*, 10297−10308.
(85) Bakr, B. W.; Sherrill, C. D. Analysis of Transition State Stabilization by Non-Covalent Interactions in Organocatalysis: Application of Atomic and Functional-Group Partitioned Symmetry-Adapted Perturbation Theory to the Addition of Organoboron Reagents to Fluoroketones. *Phys. Chem. Chem. Phys.* **2018**, *20*, 18241−18251.
(86) McDaniel, J. G.; Schmidt, J. Next-Generation Force Fields from Symmetry-Adapted Perturbation Theory. *Annu. Rev. Phys. Chem.* **2016**, *67*, 467−488.
(87) McDaniel, J. G.; Choi, E.; Son, C. Y.; Schmidt, J. R.; Yethiraj, A. Ab Initio Force Fields for Imidazolium-Based Ionic Liquids. *J. Phys. Chem. B* **2016**, *120*, 7024−7036.
(88) Son, C. Y.; McDaniel, J. G.; Schmidt, J. R.; Cui, Q.; Yethiraj, A. First-Principles United Atom Force Field for the Ionic Liquid $BMIM^+$ BF_4^-: An Alternative to Charge Scaling. *J. Phys. Chem. B* **2016**, *120*, 3560−3568.
(89) Van Vleet, M. J.; Misquitta, A. J.; Stone, A. J.; Schmidt, J. R. Beyond Born-Mayer: Improved Models for Short-Range Repulsion in ab Initio Force Fields. *J. Chem. Theory Comput.* **2016**, *12*, 3851−3870.
(90) Tafipolsky, M.; Ansorg, K. Toward a Physically Motivated Force Field: Hydrogen Bond Directionality from a Symmetry-Adapted Perturbation Theory Perspective. *J. Chem. Theory Comput.* **2016**, *12*, 1267−1279.
(91) Lao, K. U.; Herbert, J. M. A Simple Correction for Nonadditive Dispersion within Extended Symmetry-Adapted Perturbation Theory (XSAPT). *J. Chem. Theory Comput.* **2018**, *14*, 5128−5142.
(92) Lao, K. U.; Herbert, J. M. Accurate Intermolecular Interactions at Dramatically Reduced Cost: XPol+SAPT with Empirical Dispersion. *J. Phys. Chem. Lett.* **2012**, *3*, 3241−3248.
(93) Lao, K. U.; Schäffer, R.; Jansen, G.; Herbert, J. M. Accurate Description of Intermolecular Interactions Involving Ions Using Symmetry-Adapted Perturbation Theory. *J. Chem. Theory Comput.* **2015**, *11*, 2473−2486.
(94) Lao, K. U.; Herbert, J. M. Atomic Orbital Implementation of Extended Symmetry-Adapted Perturbation Theory (XSAPT) and Benchmark Calculations for Large Supramolecular Complexes. *J. Chem. Theory Comput.* **2018**, *14*, 2955−2978.
(95) Jenness, G. R.; Jordan, K. D. DF-DFT-SAPT Investigation of the Interaction of a Water Molecule to Coronene and Dodecabenzocoronene: Implications for the Water-Graphite Interaction. *J. Phys. Chem. C* **2009**, *113*, 10242−10248.
(96) Sedlak, R.; Rezác, J. Empirical D3 Dispersion as a Replacement for ab Initio Dispersion Terms in Density Functional Theory-Based

DOI: 10.1021/acs.jpca.9b06865
J. Phys. Chem. A 2019, 123, 7881−7891

Symmetry-Adapted Perturbation Theory. *J. Chem. Theory Comput.* **2017**, *13*, 1638−1646.
(97) Řezáč, J.; Hobza, P. Extrapolation and Scaling of the DFT-SAPT Interaction Energies toward the Basis Set Limit. *J. Chem. Theory Comput.* **2011**, *7*, 685−689.
(98) Hesselmann, A.; Korona, T. On the Accuracy of DFT-SAPT, MP2, SCS-MP2, MP2C, and DFT+Disp Methods for the Interaction Energies of Endohedral Complexes of the C_{60} Fullerene with a Rare Gas Atom. *Phys. Chem. Chem. Phys.* **2010**, *13*, 732−743.
(99) Misquitta, A. J.; Szalewicz, K. Symmetry-Adapted Perturbation Theory Calculations of Intermolecular Forces Employing Density-Functional Description of Monomers. *J. Chem. Phys.* **2005**, *122*, No. 214109.
(100) Sorensen, P. E.; Jencks, W. P. Acid- and Base-Catalyzed Decomposition of Acetaldehyde Hydrate and Hemiacetals in Aqueous Solution. *J. Am. Chem. Soc.* **1987**, *109*, 4675−4690.
(101) Sarrami, F.; Yu, L.-J.; Wan, W.; Karton, A. Sulphuric Acid-Catalysed Formation of Hemiacetal From Glyoxal and Ethanol. *Chem. Phys. Lett.* **2017**, *675*, 27−34.
(102) Funderburk, L. H.; Aldwin, L.; Jencks, W. P. Mechanisms of General Acid and Base Catalysis of the Reactions of Water and Alcohols with Formaldehyde. *J. Am. Chem. Soc.* **1978**, *100*, 5444−5459.
(103) Meijer, E. J.; Sprik, M. Ab Initio Molecular Dynamics Study of the Reaction of Water with Formaldehyde in Sulfuric Acid Solution. *J. Am. Chem. Soc.* **1998**, *120*, 6345−6355.
(104) Azofra, L. M.; Alkorta, I.; Elguero, J.; Toro-Labbé, A. Mechanisms of Formation of Hemiacetals: Intrinsic Reactivity Analysis. *J. Phys. Chem. A* **2012**, *116*, 8250−8259.
(105) Azofra, L. M.; Alkorta, I.; Elguero, J. A Theoretical Study of Hemiacetal Formation from the Reaction of Methanol with Derivatives of CX_3CHO (X = H, F, Cl, Br and I). *J. Phys. Org. Chem.* **2012**, *25*, 1286−1292.
(106) Politzer, P.; Burda, J. V.; Concha, M. C.; Lane, P.; Murray, J. S. Analysis of the Reaction Force for a Gas Phase SN_2 Process: $CH_3Cl + H_2O$ $CH_3OH + HCl$. *J. Phys. Chem. A* **2006**, *110*, 756−761.
(107) Rincón, E.; Toro-Labbé, A. Reaction Force and Electron Localization Function Analysis of the Metal Chelation Process in Mg(II)-Thymine Complex. *Chem. Phys. Lett.* **2007**, *438*, 93−98.
(108) Šebesta, F.; Brela, M. Z.; Diaz, S.; Miranda, S.; Murray, J. S.; Gutiérrez-Oliva, S.; Toro-Labbé, A.; Michalak, A.; Burda, J. V. The Influence of the Metal Cations and Microhydration on the Reaction Trajectory of the N3 O2 Thymine Proton Transfer: Quantum Mechanical Study. *J. Comput. Chem.* **2017**, *38*, 2680−2692.
(109) Zhao, Y.; Truhlar, D. G. The M06 Suite of Density Functionals for Main Group Thermochemistry, Thermochemical Kinetics, Noncovalent Interactions, Excited States, and Transition Elements: Two New Functionals and Systematic Testing of Four M06-Class Functionals and 12 Other Functionals. *Theor. Chem. Acc.* **2008**, *120*, 215−241.
(110) Parrish, R. M.; et al. Psi4 1.1: An Open-Source Electronic Structure Program Emphasizing Automation, Advanced Libraries, and Interoperability. *J. Chem. Theory Comput.* **2017**, *13*, 3185−3197.
(111) Smith, D. G. A.; et al. Psi4NumPy: An Interactive Quantum Chemistry Programming Environment for Reference Implementations and Rapid Development. *J. Chem. Theory Comput.* **2018**, *14*, 3504−3511.
(112) Frisch, M. J.; Pople, J. A.; Binkley, J. S. Self-Consistent Molecular Orbital Methods 25. Supplementary Functions for Gaussian Basis Sets. *J. Chem. Phys.* **1984**, *80*, 3265−3269.
(113) Weigend, F.; Ahlrichs, R. Balanced Basis Sets of Split Valence, Triple Zeta Valence and Quadruple Zeta Valence Quality for H to Rn: Design and Assessment of Accuracy. *Phys. Chem. Chem. Phys.* **2005**, *7*, 3297−3305.
(114) Ishida, K.; Morokuma, K.; Komornicki, A. The Intrinsic Reaction Coordinate. An Ab Initio Calculation for HNC→HCN and $H^- + CH_4 \rightarrow CH_4 + H^-$. *J. Chem. Phys.* **1977**, *66*, 2153−2156.
(115) Pyrex, An Open-Source Python Toolkit for Intrinsic Reactivity Analysis, 2019. For current version see, https://github.com/wderricotte/pyrex.
(116) Oliphant, T. E. *A Guide to NumPy*; Trelgol Publishing: USA, 2006; Vol. *1*.
(117) Parrish, R. M.; Gonthier, J. F.; Corminbœuf, C.; Sherrill, C. D. Communication: Practical Intramolecular Symmetry Adapted Perturbation Theory via Hartree-Fock Embedding. *J. Chem. Phys.* **2015**, *143*, No. 051103.

DOI: 10.1021/acs.jpca.9b06865
J. Phys. Chem. A 2019, 123, 7881−7891